Asian Journal of Chemistry; Vol. 38, No. 8 (2026), 2151-2162
ASIAN JOURNAL OF CHEMISTRY
https://doi.org/10.14233/ajchem.2026.36352

Reddish Orange Emitting Sm^{3+} Ion on Lithium Cadmium Orthophosphate Nanopowders for Solid State Lighting Applications

SHAIK AZAD BASHA[1], K. SRINIVASARAO[2], K. DANIEL[3], B.V. NAVEEN KUMAR[4] and SANDHYA COLE[1,*]

[1]Department of Physics, Acharya Nagarjuna University, Guntur-522510, India
[2]Department of Physics, Government Degree College, Palakonda-532440, India
[3]Department of Physics, Dr. Samuel George Institute of Engineering and Technology, Markapur-523316, India
[4]Department of Physics, University of the Free State, Bloemfontein 9300, South Africa

*Corresponding author: E-mail: sandhya.cole@gmail.com

Received: 1 May 2026 *Accepted*: 17 July 2026 *Published online*: 7 August 2026 AJC-22442

Sm^{3+}-doped $Li_2Cd_2(PO_4)_2$ (LCP) nanopowders were prepared using solid state reaction (SSR) method. Several analytical methods were used to examine the prepared samples structural, morphological, vibrational and luminous characteristics. The XRD analysis reveals that the samples were in the orthorhombic with *Pnma* space group in the nanoscale. The average crystallite size for the samples were determined using Debye Scherrer's and W-H plot methods. Surface morphology revealed an irregular stone-like clustered architecture. FT-IR and Raman spectroscopy were employed to investigate the vibrational characteristics of the samples. DRS analysis estimated optical bandgap values of 5.43 eV for the undoped sample and 5.01, 5.05, and 5.19 eV for the 0.01%, 0.05%, and 0.09% Sm^{3+}-doped LCP samples, respectively. The photoluminescence spectrum exhibited a prominent emission at 649 nm upon excitation at 401 nm. Concentration quenching behaviour, average lifetime, quantum yield, correlated colour temperature (CCT), colour purity (CP) and colour rendering index (CRI) were systematically evaluated. The optical characteristics indicate that the developed Sm^{3+}-doped LCP phosphors possess strong potential for application in reddish-orange light-emitting devices.

Keywords: $Li_2Cd_2(PO_4)_2$, Photoluminescence, Lifetime analysis, Dexter's theory.

INTRODUCTION

Nanomaterials and their big-grained counterparts are significantly more fascinating than bulk materials due to their optical, electrical and magnetic characteristics. One popular technique for preparing nanomaterials is the solid-state reaction (SSR) method [1]. Phosphors show luminosity when subjected to UV light, X-rays or other excitations [2]. The incorporation of Li^+ ions is a well-established approach for improving luminescence efficiency and enhancing emission band intensity. Li^+ ions also act as fluxing agents, promoting crystallite growth and improving crystallinity. Their incorporation increases the emission intensity of the phosphor by approximately 3.5 times. Cadmium oxide (CdO) possesses one of the highest combinations of electrical conductivity and optical transparency among metal oxides. Owing to these characteristics, CdO has attracted considerable attention for applications in photovoltaic devices, flat-panel displays, light-emitting diodes, heat-reflective coatings, smart windows, solar cells, display technologies and sensors [3].

Nanoscience has advanced considerably over the past few decades, enabling the design of complex materials and technologies through precise control of matter at the nanoscale [4,5]. Owing to their high surface-to-volume ratio, nanoparticles can significantly alter the chemical and physical properties of orthophosphate materials [6]. Spatial confinement at the nanoscale results in discrete electronic energy levels, leading to stronger optical absorption and narrower emission bands. Tailored luminescent properties can be obtained by incorporating suitable dopant ions into phosphate-based host matrices [7]. Phosphate compounds constitute an important class of materials and accommodate both trivalent and divalent cations within their crystal structures [4]. Rare-earth ions with relatively large ionic radii introduce lattice distortion and internal strain, thereby modifying the structural characteristics of the host lattice [8]. The unique optical behaviour of rare earth-

doped oxide materials originates from the partially filled 4*f* electron shell. Optical emissions arise primarily from the 4*f*-4*f* and 4*f*-5*d* electronic transitions of rare-earth ions, making these materials attractive phosphor candidates [9]. Samarium, dysprosium, neodymium and gadolinium are among the rare-earth ions frequently employed as activator dopants. Samarium is particularly attractive since it enhances ionic conductivity, charge carrier mobility and catalytic activity. Its high oxygen storage capacity, abundant oxygen vacancies and low redox potential make samarium well suited for improving the gas-sensing performance of functional materials. During crystal growth, samarium dopants can generate cation vacancies at grain boundaries through the pinning effect, thereby restricting grain boundary migration [10]. Sm_2O_3 has attracted considerable attention due to its distinctive physico-chemical properties and broad application potential in biomedicine, sensing, electronics, catalysis and related fields [11].

Rare-earth-doped materials have been synthesised using various techniques including sol-gel, hydrothermal, flame hydrolysis, chemical vapour deposition, conventional powder mixing and calcination, solid-state reaction, solution combustion synthesis and polymeric complexing [12]. Among these methods, the solid-state reaction (SSR) technique is widely employed due to its simplicity, low cost and ease of scale-up [13]. In the present study, $LiCdPO_4$ (LCP) orthophosphate nanoparticles were synthesised by the SSR method. Undoped LCP and Sm^{3+}-doped LCP nanoparticles containing 0.01, 0.05 and 0.09 mol% Sm^{3+} were prepared for systematic investigation. Crystal structure, vibrational characteristics, morphology, elemental composition, optical absorption and photoluminescence properties were examined. Concentration quenching behaviour, average lifetime, quantum yield, colour rendering index (CRI), colour purity (CP) and correlated colour temperature (CCT) were evaluated to assess the luminescence performance of the synthesised phosphors.

EXPERIMENTAL

Undoped and Sm^{3+}-doped $LiCdPO_4$ (LCP) nanoparticles containing 0.01, 0.05 and 0.09 mol% Sm^{3+} were synthesised by the solid-state reaction (SSR) method. The samples are designated as $Sm_{0.01}$, $Sm_{0.05}$ and $Sm_{0.09}$ according to the Sm^{3+} concentration. Analytical reagent (AR)-grade precursors with a purity of 99.9%, namely cadmium oxide (CdO), lithium carbonate (Li_2CO_3), samarium oxide (Sm_2O_3) and ammonium dihydrogen phosphate ($NH_4H_2PO_4$) were used as starting materials. The required amounts of each precursor were weighed according to their stoichiometric ratios and thoroughly mixed by grinding in an agate mortar with a pestle for 30 min [12].

The homogeneous mixture was calcined in a muffle furnace at 500 ºC for 2 h and allowed to cool naturally to room temperature. The calcined product was reground for 2 h to improve homogeneity before undergoing a second heat treatment at 980 ºC for 2 h [4,14]. After cooling to room temperature, the sintered material was ground again to obtain a fine powder. A schematic representation of the synthesis procedure for the undoped and Sm^{3+}-doped LCP nanoparticles is shown in Fig. 1.

Instrumentation: The P-XRD pattern for 2θ of 10º to 90º was recorded using the Malvern Panalytical Ltd. Empyrean model Powder X-Ray diffractometer at a stepwise scanning rate of 0.02º and time per step of 0.4 s for structural analysis. The wavelength of the Cu*K*α radiation employed was 1.5418 Å. The elemental analysis was conducted using INCAx-act OXFORD EDS, while the surface morphological study was conducted using the Ultra 55 ZeISS FE-SEM. The infrared spectrum between 400 and 4000 cm^{-1} was measured using the JASCO FTIR-4700 spectrometer. The Renisha in *via* Micro Raman spectrometer records Raman spectra at a resolution of 3 cm^{-1} by using a laser that excites materials at a wavelength of 532 nm. A UV-Vis-NIR spectrometer (JASCO UV V-770

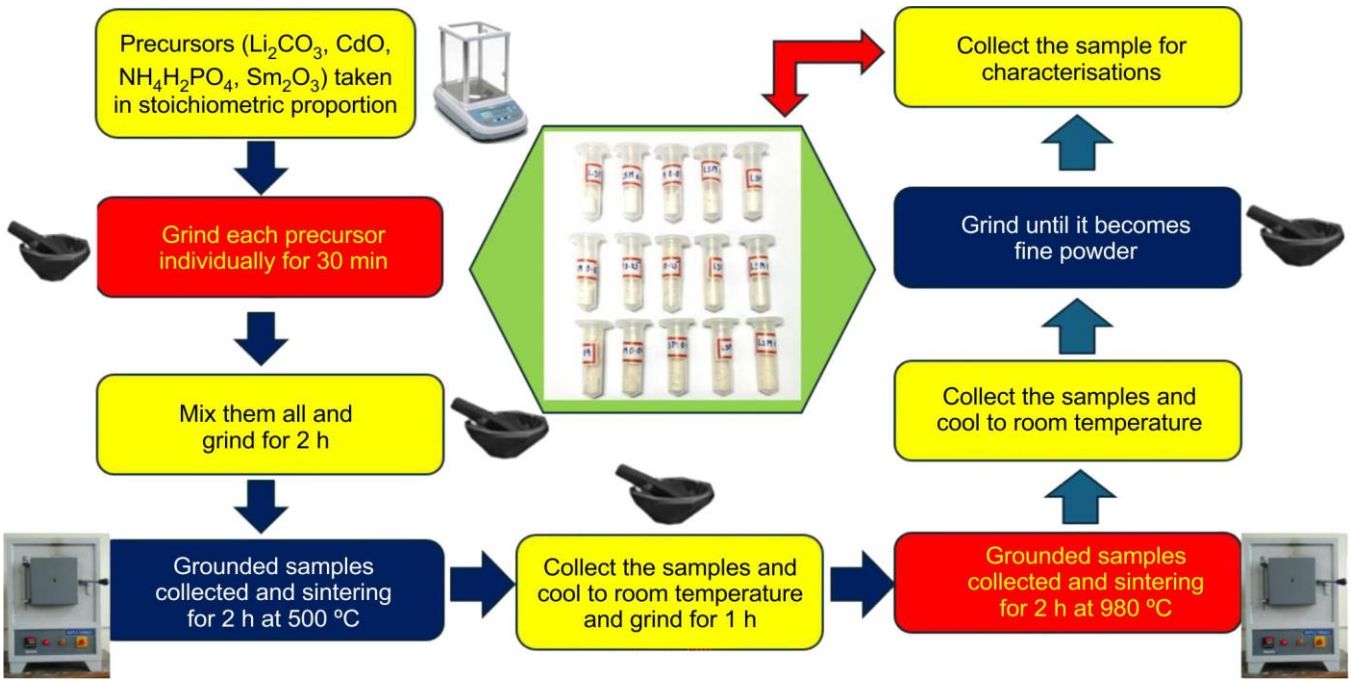

Fig. 1. Schematic representation of Sm^{3+} doped LCP NPs preparation

model) was utilised to record DRS spectra. Edinburgh Instruments FLS 980 spectrofluorometer has been used for photoluminescence studies.

RESULTS AND DISCUSSION

P-XRD studies: The crystal structure and phase purity of the synthesised samples were examined using powder X-ray diffraction (P-XRD) [12]. The diffraction patterns exhibited well-defined and sharp peaks, confirming the high crystallinity of the prepared materials. The diffraction peak positions and relative intensities agreed well with the standard data reported in JCPDS card No. 01-081-0508, confirming the formation of the $LiCdPO_4$ (LCP) phase without detectable secondary phases. The P-XRD patterns of the undoped and Sm^{3+}-doped LCP nanoparticles, together with the reference JCPDS pattern (01-081-0508), are presented in Fig. 2. Lattice parameters determined using UnitCell software are listed in Table-1 [15]. The average crystallite size was estimated using the Debye–Scherrer equation and the Williamson-Hall (W–H) method. Microstrain (ε) and dislocation density (δ) were calculated using the Stokes-Wilson (S-W) and Williamson-Smallman (W–S) relations, respectively. The calculated structural parameters, *viz*. crystallite size, microstrain, dislocation density and lattice parameters, are shown in Table-2 [16]. The corresponding Williamson–Hall plots are shown in Fig. 3.

Sm^{3+} ions are expected to substitute either Li^+ or Cd^{2+} sites within the LCP crystal lattice. The ionic radii of Li^+ (0.076 nm, CN = 6), Cd^{2+} (0.097 nm, CN = 6 or 8), and Sm^{3+} (0.096 nm, CN = 6) indicate that Sm^{3+} closely matches the size and coordination environment of Cd^{2+} [17]. Consequently, Sm^{3+} ions preferentially occupy Cd^{2+} sites in the LCP lattice. The three-dimensional polyhedral crystal structure of undoped LCP, generated using the VESTA software package, is shown in Fig. 4.

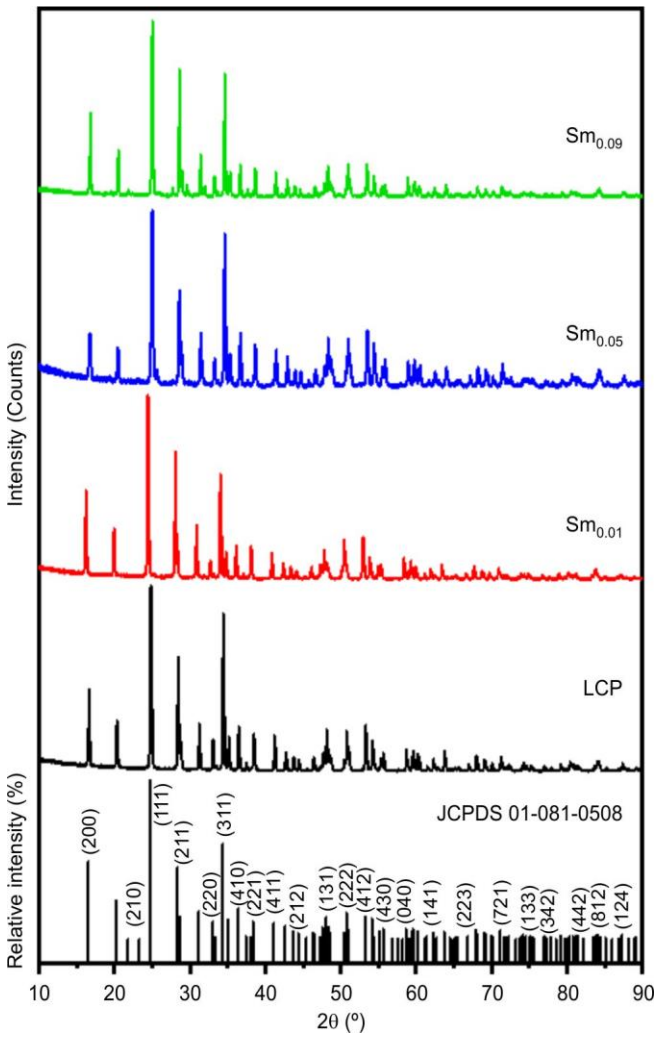

Fig. 2. P-XRD pattern of LCP NPs and JCPDS

TABLE-1
UNDOPED AND Sm^{3+} IONS DOPED LCP NPs LATTICE PARAMETERS

Parameters		JCPDS (01-081-0508)	LCP	$Sm_{0.01}$	$Sm_{0.05}$	$Sm_{0.09}$
Crystal structure		Orthorhombic	Orthorhombic	Orthorhombic	Orthorhombic	Orthorhombic
Space group		*Pnma*	*Pnma*	*Pnma*	*Pnma*	*Pnma*
Lattice parameters	a (Å)	10.7240	11.0565	10.8122	10.6085	10.6013
	b (Å)	6.2880	6.2334	6.3636	6.2467	6.2347
	c (Å)	4.8040	4.7750	4.8319	4.7890	4.7514
	α (°)	90.0000	90.0000	90.0000	90.0000	90.0000
	β (°)	90.0000	90.0000	90.0000	90.0000	90.0000
	γ (°)	90.0000	90.0000	90.0000	90.0000	90.0000
Volume ($Å^3$)		323.95	329.10	332.46	317.36	314.04

TABLE-2
COMPARISON OF VARIOUS NPs STRUCTURAL PARAMETERS LIKE D, ε, δ, LATTICE STRUCTURE AND PHASE SPACE GROUP

Sample	Debye Scherrer's method			W-H plot method			Lattice structure	Phase space group
	Crystallite size (D, nm)	Micro strain (ε)	Dislocation density (δ) (lines/m^2)	Crystallite size (D, nm)	Micro strain (ε)	Dislocation density (δ) (lines/m^2)		
LCP	31.49	25.40×10^{-4}	1.008×10^{15}	32.17	82.33×10^{-4}	0.966×10^{15}	Orthorhombic	*Pnma*
$Sm_{0.01}$	32.73	44.80×10^{-4}	0.933×10^{15}	31.08	78.80×10^{-4}	1.035×10^{15}		
$Sm_{0.05}$	33.05	35.00×10^{-4}	0.915×10^{15}	32.47	34.27×10^{-4}	0.948×10^{15}		
$Sm_{0.09}$	33.98	40.72×10^{-4}	0.866×10^{15}	33.57	29.56×10^{-4}	0.887×10^{15}		

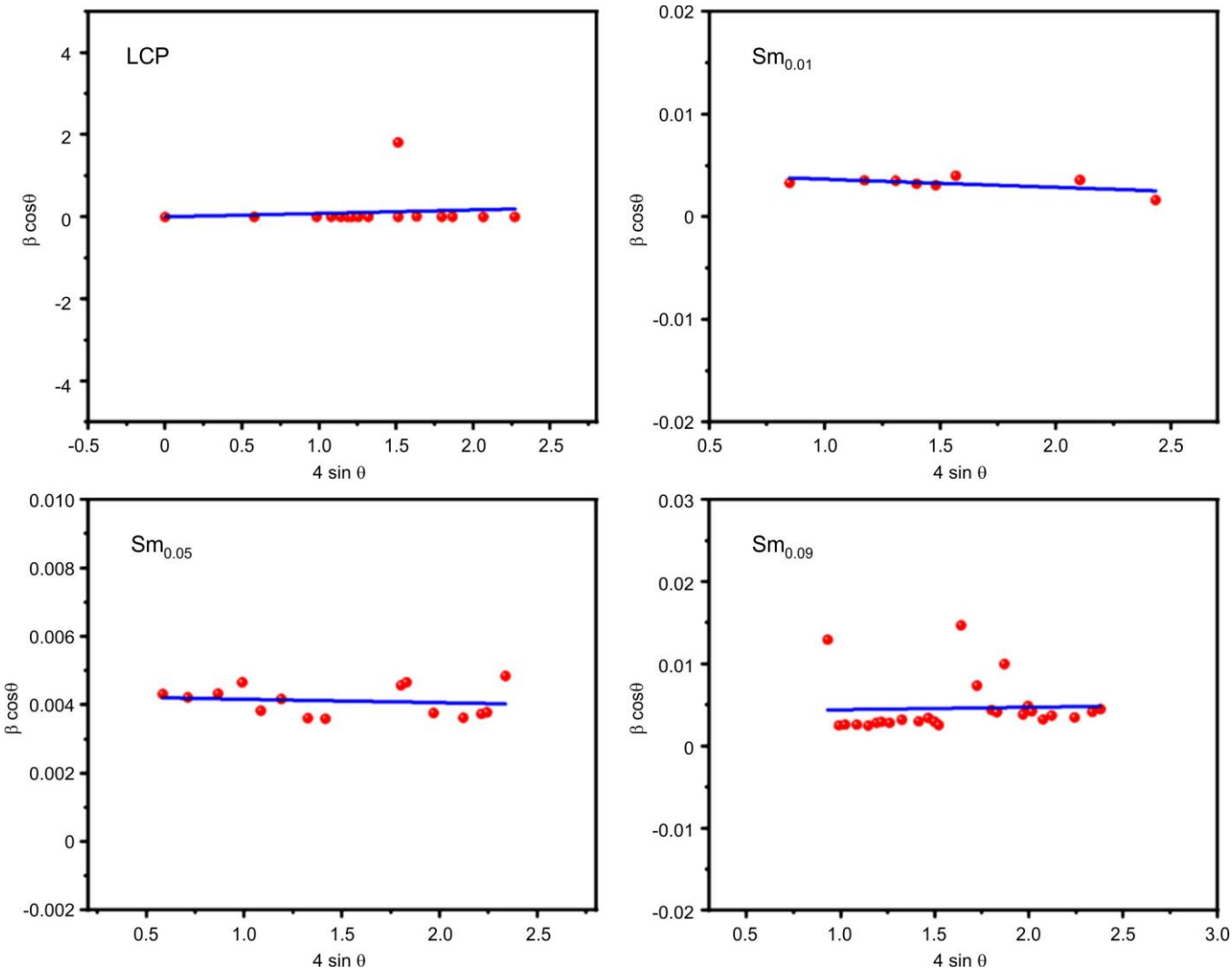

Fig. 3. W-H Plot of LCP NPs

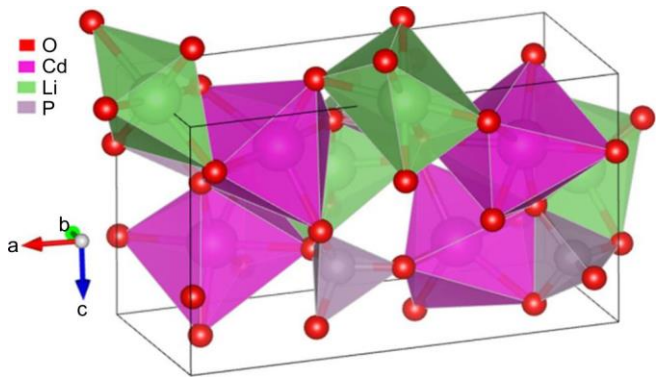

Fig. 4. Polyhedral 3D crystal structure diagram of undoped LCP NPs

Substitution of Sm^{3+} for Cd^{2+} introduces one excess positive charge for each replacement. Charge compensation is therefore achieved through the formation of cadmium vacancies. Two Sm^{3+} ions occupying Cd^{2+} sites are compensated by one cadmium vacancy, which is energetically more favourable than the formation of interstitial defects or oxygen vacancies. This substitution mechanism is supported by the close agreement in ionic radius and coordination number between Sm^{3+} and Cd^{2+}, making Cd^{2+} sites more favourable than the comparatively smaller Li^{+} sites. Local lattice relaxation associated with cadmium vacancies and the slightly smaller effective ionic radius of Sm^{3+} compared with Cd^{2+} further stabilise the crystal structure at higher dopant concentrations [17,18].

Morphology studies and EDS analysis: Field-emission scanning electron microscopy (FE-SEM) was employed to examine the surface topography, particle morphology, grain size, and growth characteristics of the synthesised samples. FE-SEM micrographs of the Sm^{3+} -doped LCP nanoparticles are shown in Fig. 5. The synthesised nanoparticles exhibit an irregular clustered stone-like morphology. The average particle size was estimated from FE-SEM images recorded at a resolution of 200 nm, and the corresponding particle size distribution histogram is shown in Fig. 6. Grain size analysis was carried out by measuring 50 representative particles using ImageJ software [19].

Energy-dispersive X-ray spectroscopy (EDS) was used to determine the elemental composition of the Sm^{3+}-doped LCP nanoparticles. The spectra confirmed the presence of Sm, Cd, P and O, with atomic percentages closely matching the nominal compositions, as shown in Fig. 7. Lithium could not

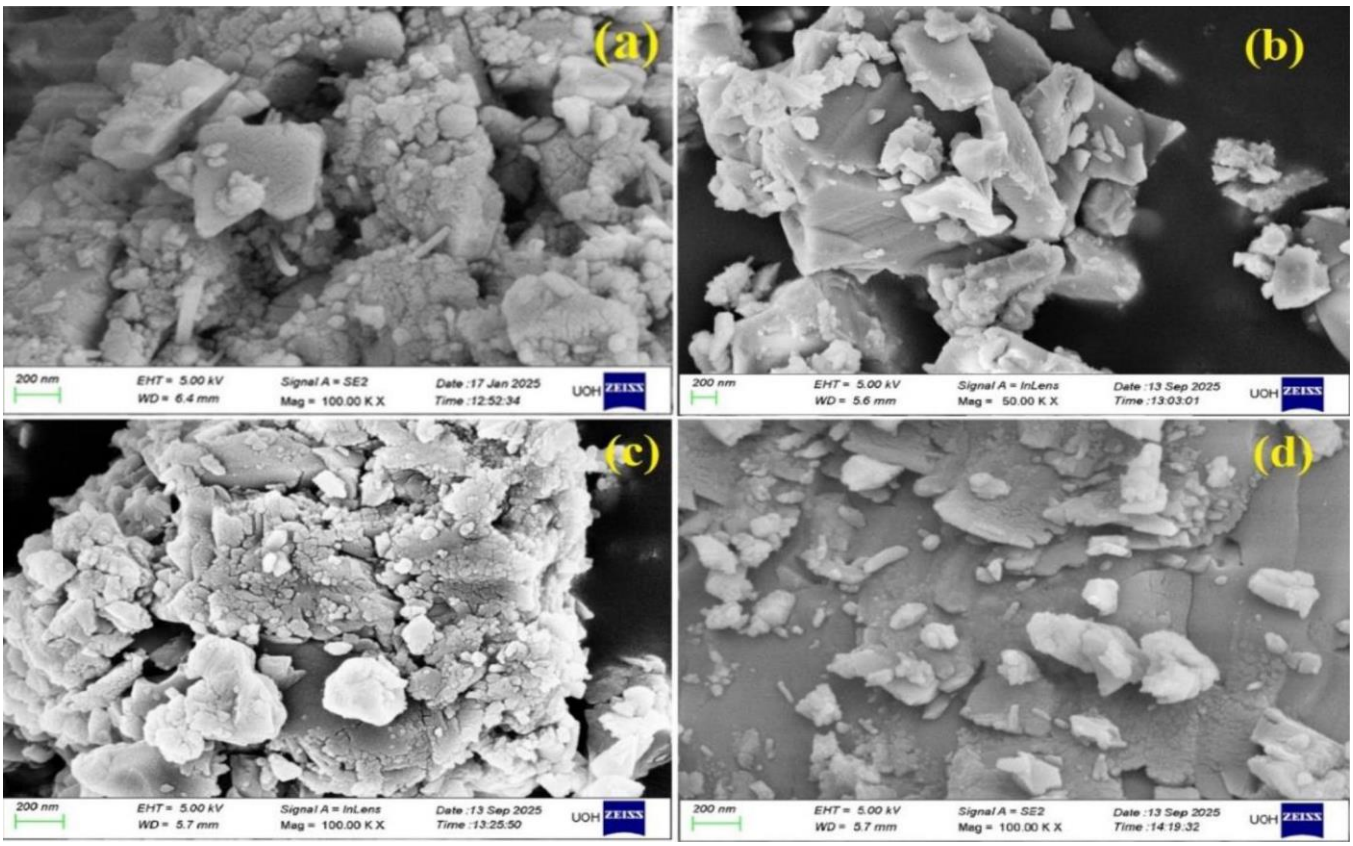

Fig. 5. FE-SEM images of (a) LCP, (b) $Sm_{0.01}$, (c) $Sm_{0.05}$ and (d) $Sm_{0.09}$

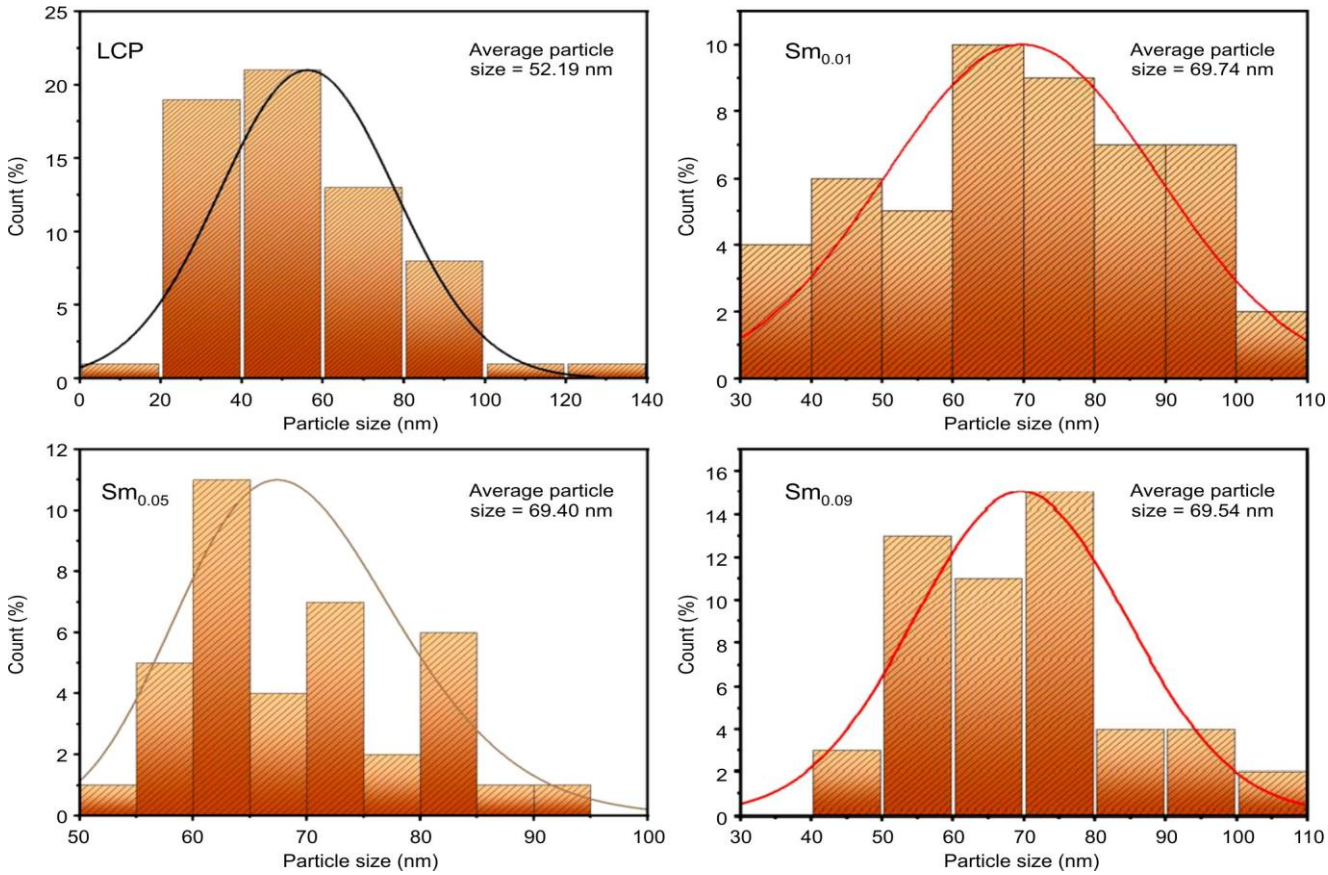

Fig. 6. Average particle size histograms of LCP, $Sm_{0.01}$, $Sm_{0.05}$ and $Sm_{0.09}$

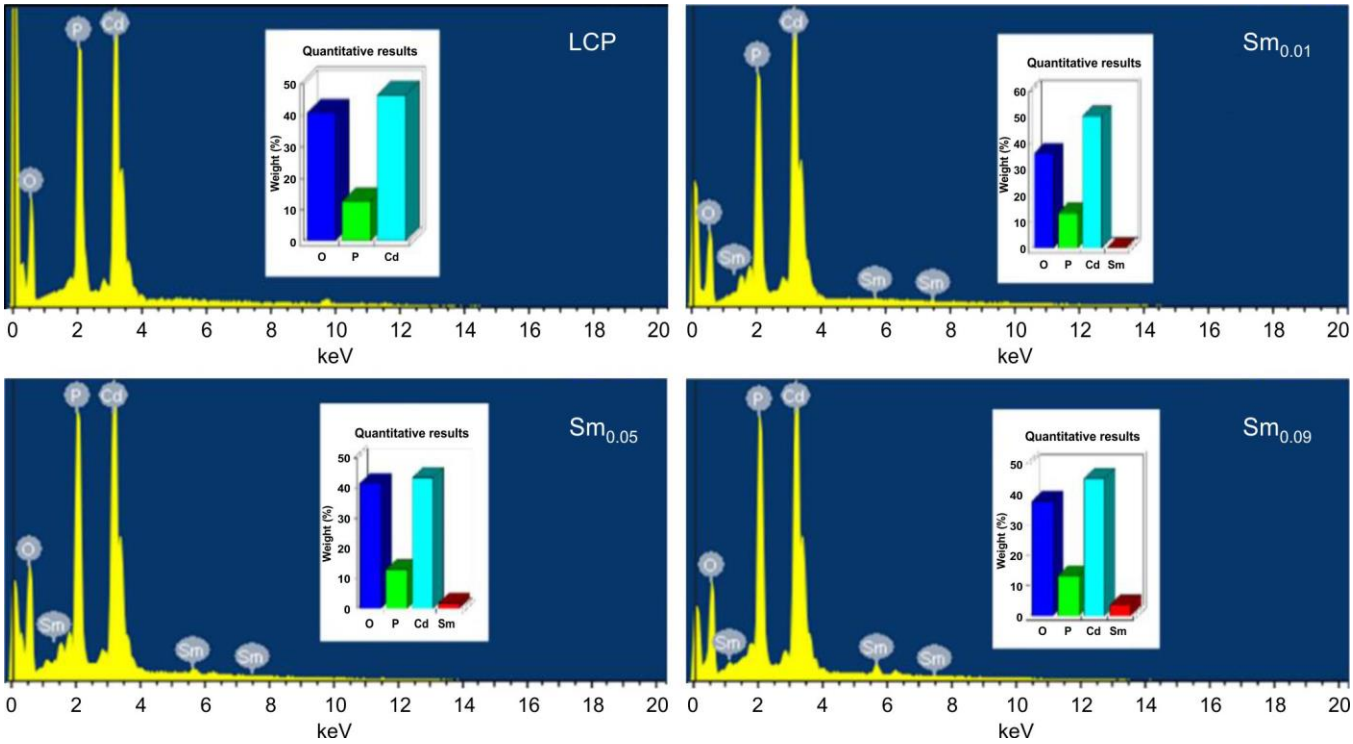

Fig. 7. EDS elemental compositions of LCP, $Sm_{0.01}$, $Sm_{0.05}$ and $Sm_{0.09}$

be detected by conventional EDS due to its low atomic number (Z < 3), coupled with strong absorption effects arising from the surrounding heavier elements and surface layers [20]. The average particle size of the synthesised samples is shown in Table-3.

TABLE-3
AVERAGE PARTICLE SIZE OF UNDOPED AND Sm^{3+} DOPED LCP NPs

Compound	Average particle size (nm)
LCP	52.19
$Sm_{0.01}$	69.74
$Sm_{0.05}$	69.40
$Sm_{0.09}$	69.54

FT-IR analysis: The FT-IR spectra of the undoped and Sm^{3+}-doped LCP nanoparticles recorded over the range of 4000-400 cm^{-1} are shown in Fig. 8. All samples exhibit similar absorption bands, confirming that Sm^{3+} incorporation does not alter the fundamental framework of the LCP host lattice. The weak absorption band observed near 2971-2839 cm^{-1} is assigned to C–H stretching vibrations originating from the residual surface species. The absorption bands observed in the 2363-2350 cm^{-1} region appear from atmospheric CO_2 absorbed during FT-IR measurements. The absorption bands appearing between 1747 and 1733 cm^{-1} are associated with C=O stretching vibrations, while those near 1373-1360 cm^{-1} correspond to carbonate-related vibrations. The prominent absorption bands located at 1135-1133 and 1045-1031 cm^{-1} appears from the asymmetric stretching vibrations (ν_3) of the PO_4^{3-} tetrahedra. The bands centred at 957-951 cm^{-1} are assigned to the symmetric stretching mode (ν_1) of the phosphate

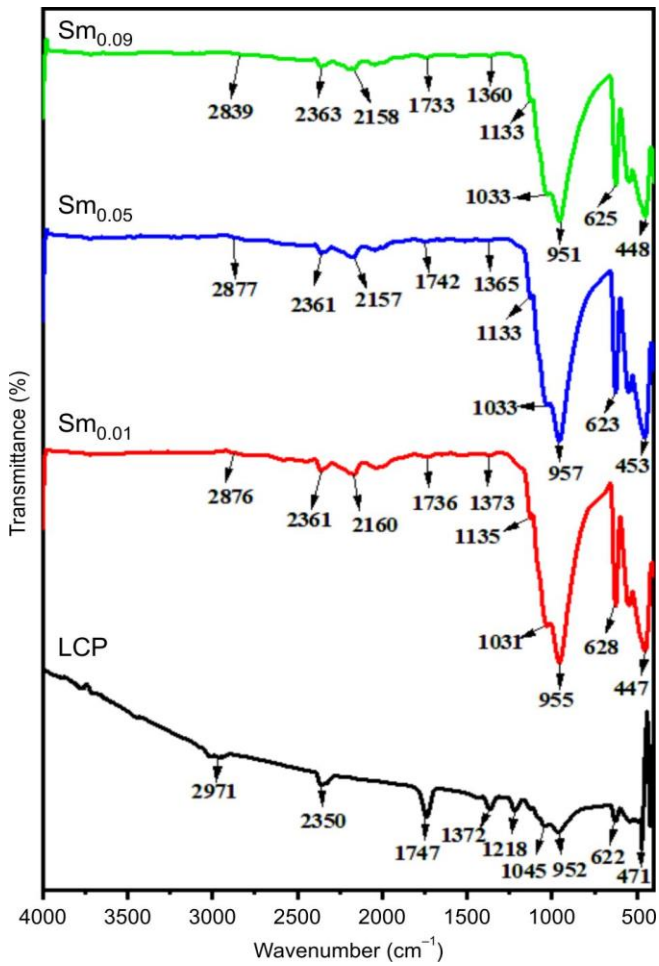

Fig. 8. FT-IR spectra of undoped and Sm^{3+} doped LCP nanopowders

TABLE-4
RAMAN BAND ASSIGNMENTS OF Sm^{3+} DOPED LCP NPs

Wavenumber (cm^{-1})				Assignments
LCP	$Sm_{0.01}$	$Sm_{0.05}$	$Sm_{0.09}$	
216	300	–	–	External modes
444	438	442	429	δ_s (PO_4)
609	623	622	617	δ_{as} (PO_4)
957	947	946	947	ν_s (PO_4)
1010, 1076	1030, 1112	1027, 1107	1026, 1110	ν_{as} (PO_4)
1320	1382	1382	1384	External modes

group. The absorption bands in the 628-622 cm^{-1} region originate from the O–P–O bending vibrations (ν_4), whereas the low-wavenumber bands observed between 471 and 447 PO_4^{3-} correspond to the bending mode (ν_2) of PO_4^{3-} units. Minor shifts in the band positions with increasing Sm^{3+} concentration may be attributed to local lattice distortion arising from substitution of Cd^{2+} by Sm^{3+} ions. No additional absorption bands corresponding to impurity phases are observed, supporting the phase purity of the synthesised LCP nanoparticles [21].

Raman analysis: Raman spectroscopy serves as an effective technique for investigating lattice vibrations, structural defects and disorder in nano- and microstructured materials [22]. The Raman spectra recorded in the 200-1300 cm^{-1} region exhibit symmetric and asymmetric vibrational modes of the PO_4^{3-} tetrahedra, consistent with the FT-IR results. A prominent Raman band centred at 957 cm^{-1} is assigned to the symmetric stretching vibration of the PO_4^{3-} group. The Raman spectra of the Sm^{3+}-doped LCP nanoparticles are shown in Fig. 9 and the corresponding vibrational mode assignments are shown in Table-4.

DRS analysis: The diffuse reflectance spectra (DRS) of the undoped and Sm^{3+}-doped LCP nanoparticles were recorded over the wavelength range of 200-800 nm [12]. Strong absorption was observed in the UV region (250-350 nm). The DRS spectra of the undoped and Sm^{3+}-doped LCP samples are shown in Fig. 10. The optical bandgap was determined from the Kubelka-Munk (KM) function by plotting $[F(R)h\nu]^n$ *versus* photon energy ($h\nu$) [23]. The estimated optical bandgap values for the undoped, 0.01, 0.05, and 0.09 mol% Sm^{3+}-doped LCP samples are 5.43, 5.01, 5.05 and 5.19 eV, respectively, and are shown in Table-5. The corresponding KM plots are shown in Fig. 11. The wide optical bandgap of the synthesised LCP nanoparticles makes them promising candidates for solid-state lighting applications [24].

TABLE-5
ENERGY BAND GAP OF NANOPOWDERS SAMPLES

Sample	Band gap (eV)
LCP	5.43
$Sm_{0.01}$	5.01
$Sm_{0.05}$	5.05
$Sm_{0.09}$	5.19

Photoluminescence studies: The excitation spectra of the Sm^{3+}-doped LCP nanoparticles are shown in Fig. 12. Several excitation bands appear in the 350-500 nm region when monitored at an emission wavelength of 649 nm. These bands

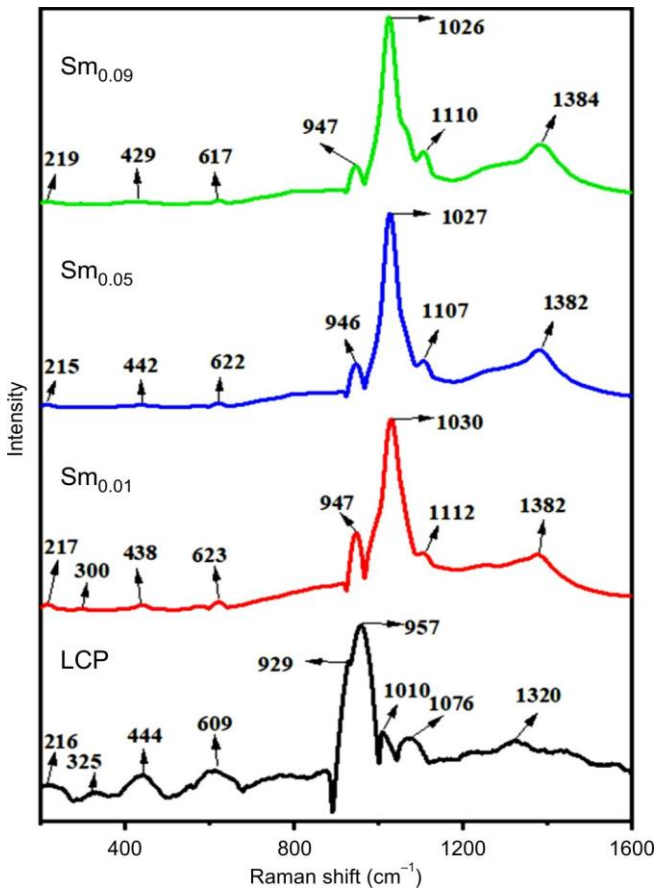

Fig. 9. Raman spectra of LCP NPs

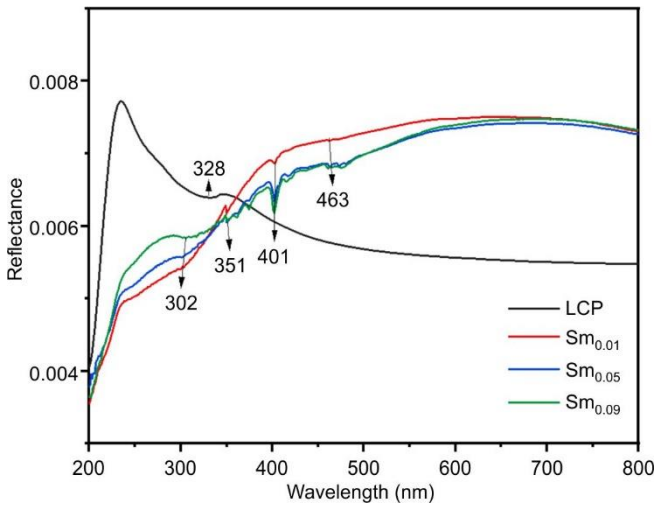

Fig. 10. DRS spectra of undoped and Sm^{3+} doped LCP NPs

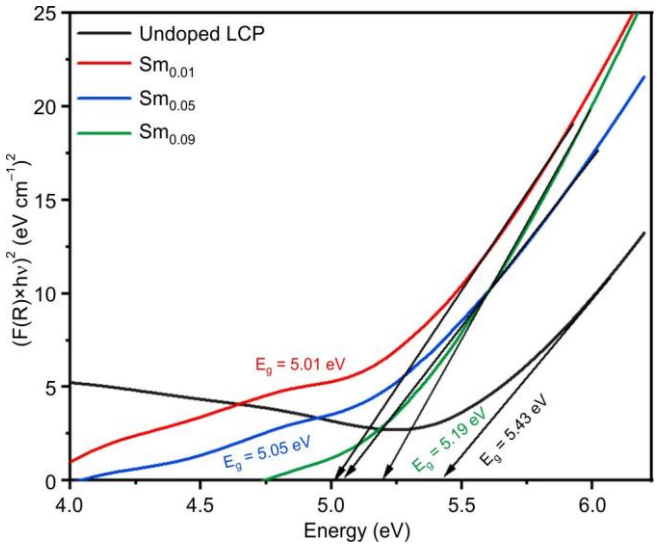

Fig. 11. Energy band gaps of samples

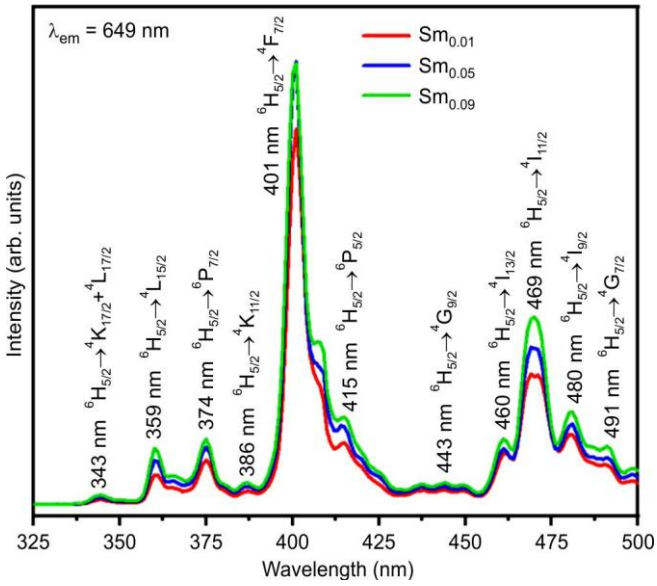

Fig. 12. PL excitation spectra of Sm^{3+} doped LCP NPs

arise from the intra-configurational 4*f*-4*f* transitions of Sm^{3+} ions. The most intense excitation band occurs at 401 nm, corresponding to the $^6H_{5/2} \rightarrow {}^4F_{7/2}$ transition. Other excitation bands are observed at 343, 359, 374, 386, 415, 443, 460, 469, 480 and 491 nm, each corresponding to characteristic electronic transitions of Sm^{3+} ions (Fig. 12). The intense excitation at 401 nm matches well with the emission of near-ultraviolet (NUV) LED chips, making the Sm^{3+}-doped LCP phosphor a suitable candidate for phosphor-converted white light-emitting diode (pc-LED) applications [25].

The emission spectra of the Sm^{3+}-doped LCP nanoparticles recorded under 401 nm excitation are shown in Fig. 13. Four characteristic emission bands are observed at 562, 600, 649 and 712 nm, initiating from the $^4G_{5/2} \rightarrow {}^6H_{5/2}$, $^4G_{5/2} \rightarrow {}^6H_{7/2}$, $^4G_{5/2} \rightarrow {}^6H_{9/2}$ and $^4G_{5/2} \rightarrow {}^6H_{11/2}$ transitions of Sm^{3+} ions, respectively [26,27]. Among these transitions, the emission centred at 649 nm is attributed to the electric-dipole ($^4G_{5/2} \rightarrow {}^6H_{9/2}$) transition and is responsible for the intense red luminescence observed in the synthesized phosphor [28].

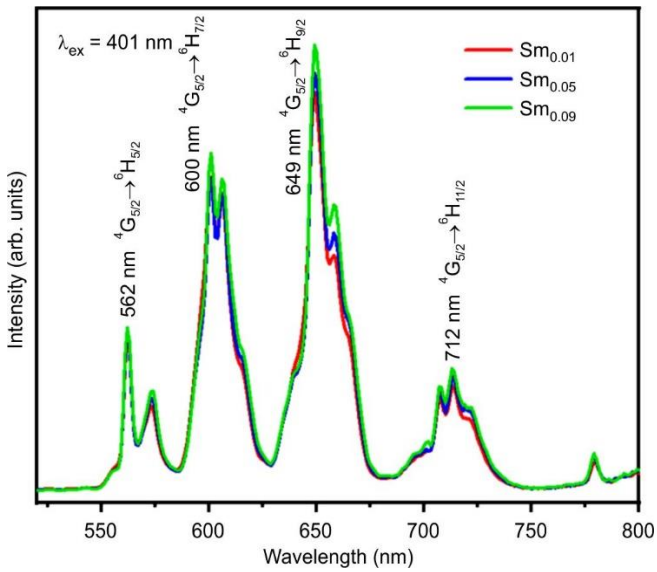

Fig. 13. PL emission spectra of Sm^{3+} doped LCP NPs

The emission intensity reaches a maximum at 0.05 mol% Sm^{3+} and decreases with further increase in dopant concentration because of concentration quenching. As the Sm^{3+} content increases, neighbouring activator ions come closer together, allowing non-radiative energy transfer through cross-relaxation. This process may proceed through exchange or multipolar interactions. The nature of the interaction was examined by calculating the critical transfer distance (R_c). An R_c value below 5 Å corresponds to exchange interaction, whereas a value above 5 Å is associated with multipolar interaction [29,30]. The critical transfer distance was estimated using the Blasse equation (eqn. 1):

$$R_c = 2\left(\frac{3V}{4\pi Z X_c}\right)^{1/3} \qquad (1)$$

where X_c (0.05%) is the optimal concentration of Sm^{3+} ions in the host matrix, Z is the number of accessible cationic sites and V (317.36 $Å^3$) is the unit cell's volume. Since the calculated value of R_c is 14.50 Å, which is more than 5 Å, multipolar contact is responsible for the energy migration between Sm^{3+}-Sm^{3+} ions. Dexter's concept was used to identify the kind of multipolar interaction that leads to concentration quenching. The kind of multipolar interaction can be ascertained using eqn. 2:

$$\frac{1}{X} = k\left[1+\beta(X)^{Q/3}\right]^{-1} \qquad (2)$$

where X = Sm^{3+} concentration is either equal to or higher than the ideal concentration; I = integrated intensity; Q = multipolar interaction type; and k and β are the constants. Q = 6, 8 and 10 stands for dipole-dipole, dipole-quadrupole and quadrupole-quadrupole interactions [31]. The equation above reduces to eqn. 3:

$$\log\left(\frac{I}{X}\right) = C - \frac{Q\log(X)}{3} \qquad (3)$$

where C = log k - logβ.

Fig. 14 displays log (I/X) *vs.* log (X) plots. The analysed data are fitted linearly (R^2 = 0.999), with a slope (-Q/3) of

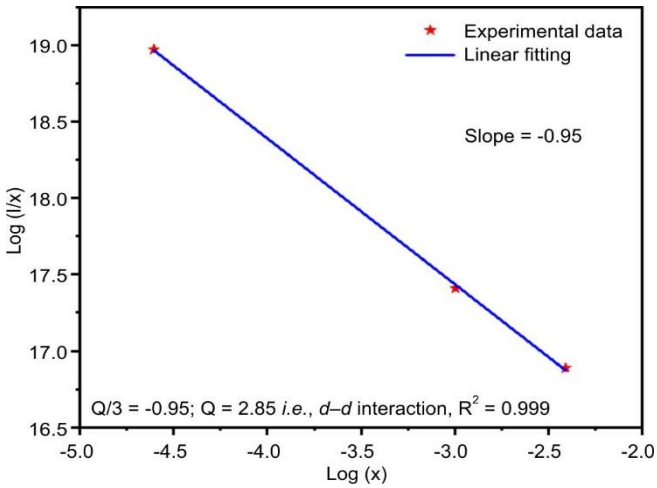

Fig. 14. Fitting curve in the plot of log (I/x) *vs.* log (x) in Sm^{3+} doped LCP NPs

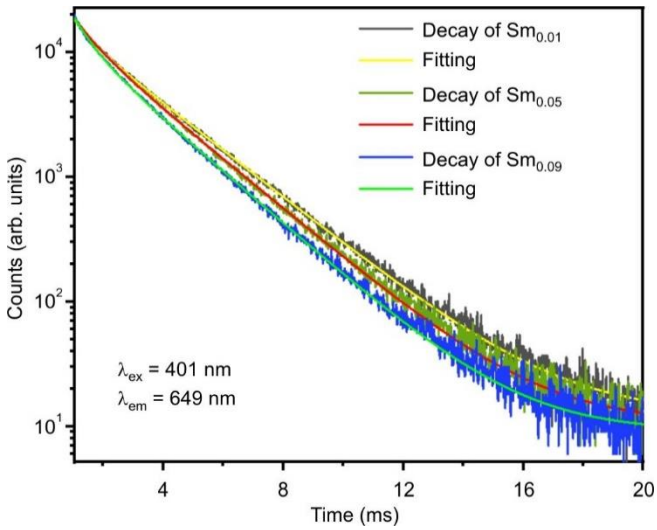

Fig. 16. Lifetime plots of Sm^{3+} doped LCP NPs

-0.95. The calculated Q value of 2.85 is much closer to 6 than to the other theoretical values. Based on the Dexter's theory, concentration quenching in the Sm^{3+}-doped LCP nanoparticles is governed by dipole-dipole interaction. The intensity reduction at 0.05% confirms concentration quenching [25,32, 33]. In trivalent rare earth ions, electronic transitions in crystalline nature usually prefer multiplet-to-multiplet transitions. The absence of an inversion center near the Sm^{3+} ion is necessary for the electric dipole (ED) transition to be induced. Moreover, the local environment symmetry of Sm^{3+} ions has a significant impact on the magnitude of the transformation. An energy level diagram of Sm^{3+} doped LCP NPs is shown schematically in Fig. 15.

The lifetime decay curves of the Sm^{3+} doped LCP NPs samples Are shown in Fig. 16. Eqn. 4 was used to fit each prepared sample's decay curves with a double-exponential function. The determined decay values are found to be 2.010 ms, 2.180 ms, 1.862 ms, respectively for the prepared samples. The average lifetime values increase first from 2.010 ms ($Sm_{0.01}$) to 2.180 ms ($Sm_{0.05}$) and later decrease to 1.862 ms ($Sm_{0.09}$). The initial increase is due to the decreasing number of non-radiative de-excitations at the surface/defect area as the crystallinity level and Sm^{3+} incorporation frequency goes on increasing up to the optimal concentration, whereas the decrease of the life time after 0.05% is attributed due to the beginning of concentration quenching by the dipole, dipole-mediated Sm^{3+}-Sm^{3+} energy transfer [31,34].

$$\tau = \frac{A_1\tau_1^2 + A_2\tau_2^2}{A_1\tau_1 + A_2\tau_2} \quad (4)$$

An essential metric for evaluating the photoluminescence efficiency of the phosphor material is the photoluminescence quantum yield (PLQY). The ratio of photons released to all photons absorbed under specific excitation circumstances is known as the quantum yield in mathematics [35]. An integrating sphere inside the FLS980 spectrometer was used to measure the PLQY. The 120 mm PTFE integrating sphere has a reflectance of about 95% in the 250-2500 nm spectral range and 99% in the 400-1500 nm range. A sample in the integrating sphere and incident beam path was utilised for direct measurement. A reflective PTFE standard is loaded without a sample is the integrating sphere [36,37]. The photoluminescence quantum yield (PLQY) was calculated using eqn. 5 and a value of 4% was obtained. The PLQY spectrum of the LCP:0.09 mol% Sm^{3+} sample recorded under 401 nm excitation is shown in Fig. 17 [38,39].

$$\text{PLQY } (\%) = \frac{Em_2 - Em_1}{Ex_1 - Ex_2} \quad (5)$$

where Ex_1, Ex_2 and Em_1, Em_2 denote, respectively, the quantity of photons in the excitation wavelength for the empty sphere calculation and the number of photons in the emission wavelength area for the measurement of an empty sphere and the sample in the sphere placed in the light beam's path.

Photometric analysis: Fig. 18 displayed the CIE chromaticity diagram of Sm^{3+} doped LCP NPs. Table-6 lists the

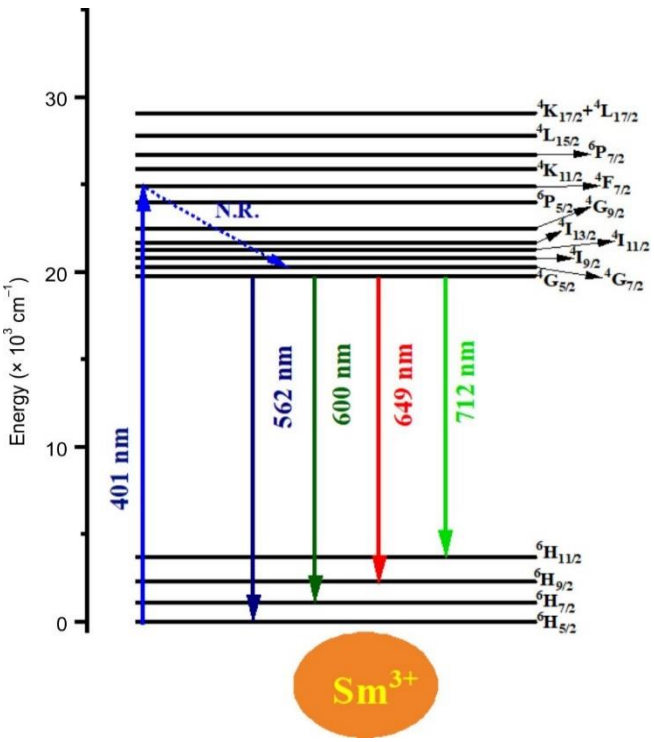

Fig. 15. Schematic energy level diagram of Sm^{3+} doped LCP NPs

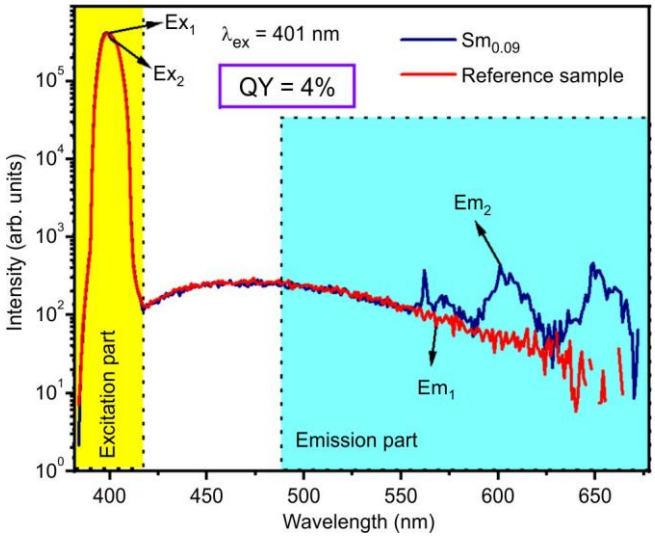

Fig. 17. Photoluminescence quantum yield (PLQY) graphs of LCP: 0.09% Sm^{3+} sample for λ_{ex} = 401 nm

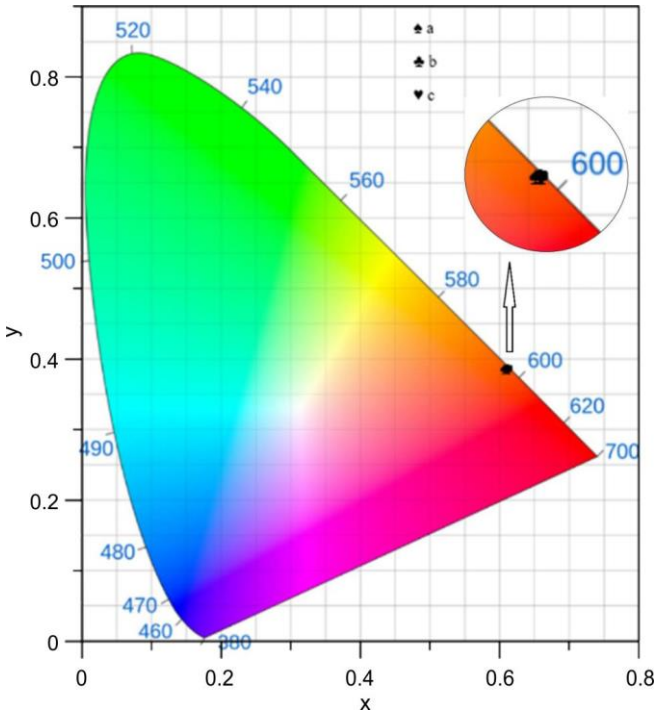

Fig. 18. CIE chromaticity diagram of (a) $Sm_{0.01}$, (b) $Sm_{0.05}$ and (c) $Sm_{0.09}$

photometric parameters of the synthesized samples, namely the CIE chromaticity coordinates, correlated colour temperature (CCT), colour purity (CP), and colour rendering index (CRI), obtained from CIE OSRAM software [40]. The CIE coordinates of the 0.01, 0.05, and 0.09 mol% Sm^{s}-doped LCP samples are (0.6067, 0.3853), (0.6095, 0.3849) and (0.6117, 0.3841), respectively. All three compositions are located in the reddish-orange region of the CIE chromaticity diagram [41].

When analysing emission spectrum data, the CRI is an essential photometric statistic. According to the CRI value, Sm^{3+} doped LCP NPs have clean emission characteristics. The photometric characteristics obtained in this study support the application of the Sm^{3+}-doped LCP phosphors in high-density optical data storage, colour display systems, light-emitting diodes (LEDs) and warm light-emitting photo-responsive devices [42]. The reddish-orange emission exhibited by the synthesised phosphors further supports their suitability for LED lighting and related photonic applications.

Conclusion

Undoped and Sm^{3+}-doped $LiCdPO_4$ (LCP) nanoparticles containing 0.01, 0.05 and 0.09 mol% Sm^{3+} were successfully synthesised by the solid-state reaction (SSR) method. Powder X-ray diffraction confirmed the formation of a single-phase crystalline LCP structure without detectable impurity phases. The crystallite sizes, estimated using the Debye-Scherrer equation and Williamson–Hall analysis, ranged from 31 to 33 nm. FE-SEM examination showed an irregular clustered stone-like morphology, while the average particle size was obtained from particle size distribution analysis. Energy-dispersive X-ray spectroscopy verified the presence of the constituent elements in the synthesised phosphors. FT-IR and Raman spectroscopy established the characteristic vibrational modes of the phosphate (PO_4^{3-}) groups. Diffuse reflectance measurements yielded optical bandgap values of 5.43, 5.01, 5.05, and 5.19 eV for the undoped, 0.01, 0.05 and 0.09 mol% Sm^{3+}-doped LCP samples, respectively. Photoluminescence studies identified a strong excitation band at 401 nm ($^6H_{5/2} \rightarrow {}^4H_{7/2}$) and a prominent reddish-orange emission centred at 649 nm ($^4G_{5/2} \rightarrow {}^6H_{9/2}$). The maximum emission intensity was obtained for the 0.05 mol% Sm^{3+}-doped sample, while higher dopant concentrations led to concentration quenching through multipolar interaction. Luminescence lifetime, photoluminescence quantum yield (PLQY), concentration quenching behaviour, colour purity (CP), correlated colour temperature (CCT) and colour rendering index (CRI) were evaluated to assess the optical performance of the synthesised phosphors. The CIE chromaticity coordinates lie in the reddish-orange region,

TABLE-6
COMPARATIVE PHOTOMETRIC PARAMETERS OF Sm^{3+} DOPED LCP NPs

Compound	CIE colour coordinates (x,y)	Colour purity (%)	CRI (%)	CCT (K)	Ref.
$Sm_{0.01}$	(0.6067, 0.3853)	97.7	50	1359	
$Sm_{0.05}$	(0.6095, 0.3849)	98.5	51	1344	Present work
$Sm_{0.09}$	(0.6117, 0.3841)	98.9	50	1330	
MCP:$Sm_{0.01}$	(0.4356, 0.5338)	91.1	43	3817	
MCP:$Sm_{0.05}$	(0.4272, 0.5405)	90.6	43	3966	[23]
MCP:$Sm_{0.1}$	(0.4183, 0.5471)	90.0	38	4078	
Sm^{3+} doped $Cd_2Sr(PO_4)_2$	(0.5097, 0.4748)	95.6	58	2546	[4]
Sm^{3+} doped $Ba_2ZnSi_2O_7$	(0.6042, 0.3951)	100	–	1416	[30]

demonstrating good colour characteristics for lighting applications. The combined structural, optical and photometric results establish Sm^{3+}-doped LCP phosphors as promising materials for reddish-orange solid-state lighting, phosphor-converted light-emitting diodes (pc-LEDs), colour display technologies, and other photonic devices.

CONFLICT OF INTEREST

The authors declare that there is no conflict of interests regarding the publication of this article.

DECLARATION OF AI-ASSISTED TECHNOLOGIES

During the preparation of this manuscript, the authors used an AI-assisted tool(s) to improve the language and no data, results or scientific conclusions were generated by AI. All analyses, interpretations and conclusions are the authors' own. The authors reviewed and edited the content and take full responsibility for the published work.

REFERENCES

1. K. Poria, S. Bhatia, R. Kashyap, V. Kashyap, I. Sihmar, N. Deopa and J.S. Shahi, *RSC Adv.*, **14**, 29490 (2024); https://doi.org/10.1039/D4RA05026F
2. Y. Zhang, Y. Liang, F. Liu and X.-J. Wang, *Light Sci. Appl.*, **15**, 220 (2026); https://doi.org/10.1038/s41377-026-02276-8
3. Z. Sun, Y. Zhou and M. Li, *J. Mater. Res.*, **23**, 732 (2008); https://doi.org/10.1557/JMR.2008.0085
4. A. Bradicich, C. R. Allemang, S. Addamane, S.D. House, A. Chen, J. Yoo, E. Bussmann, C.M. Smyth, P. Maksymovych, S. Neumayer, M. Checa, O. Dyck, L. Basso, P. Kehayias, A.M. Mounce, C. F. Doiron, M.T. Pettes, N. Li, J. Wen, L. Yates, A. Jarzembski, C.T. Harris, C.-Y. Nam, M. Titze, L. Hackett, A. Wali, A.V. Sumant, P. Iyer, C. Jozwiak, W. Pan, R. Ruiz, R. Dingreville, J.S. Nelson and T.-M. Lu, *Appl. Phys. Rev.*, **12**, 041308 (2025); https://doi.org/10.1063/5.0283106
5. M. Elansary, M. Belaiche, C. Ahmani Ferdi, E. Iffer and I. Bsoul, *RSC Adv.*, **10**, 25239 (2020); https://doi.org/10.1039/D0RA04722H
6. P.D. Solanki, M.H. Oza, G. Joshi, H.O. Jethva and M.J. Joshi, *ECS J. Solid State Sci. Technol.*, **12**, 031001 (2023); https://doi.org/10.1149/2162-8777/acbc98
7. R. Mahajan and R. Prakash, *J. Mater. Sci. Mater. Electron.*, **33**, 25491 (2022); https://doi.org/10.1007/s10854-022-09279-2
8. G. Sharada, G. Thirupathi, G. Shwetha, N.P. Kumar, P. Sowjanya and D. Sreenivasu, *ECS J. Solid State Sci. Technol.*, **12**, 063006 (2023); https://doi.org/10.1149/2162-8777/acde0e
9. S. Sisira, L.A. Jacob, K. Thomas, D. Alexander, P.R. Biju, N.V. Unnikrishnan and C. Joseph, *J. Lumin.*, **209**, 197 (2019); https://doi.org/10.1016/j.jlumin.2019.01.043
10. G.A. Babu, S. Gowthami, E. Varadarajan, B. Rawal and B. Praveenkumar, *J. Mater. Sci. Mater. Electron.*, **32**, 3264 (2021); https://doi.org/10.1007/s10854-020-05075-y
11. M.M. Antoinette, S. Israel, A.J. Amali, J.L. Berchmans, B.S. Kumar, G.J. Manoj and U.M. Usmaniya, *Nano-Struct. Nano-Objects*, **13**, 51 (2018); https://doi.org/10.1016/j.nanoso.2017.12.001
12. A.S. Patil, A.V. Patil, C.G. Dighavkar, V.A. Adole and U.J. Tupe, *Chem. Phys. Lett.*, **796**, 139355 (2022); https://doi.org/10.1016/j.cplett.2022.139355
13. A. Rajendrakumar, N.C. Anjaneyulu, G. Vasu, R.V.S.S.N. Ravikumar and N. Arundhathi, *J. Mater. Sci. Mater. Electron.*, **34**, 1958 (2023); https://doi.org/10.1007/s10854-023-11350-5
14. K. Daniel, B.V.N. Kumar, Y.N. Rajeev, K. Venkatarao and S. Cole, *Physica E*, **159**, 115911 (2024); https://doi.org/10.1016/j.physe.2024.115911
15. X.Z. Li, *Ultramicroscopy*, **102**, 269 (2005); https://doi.org/10.1016/j.ultramic.2004.10.008
16. G.R. Rani, S. Kuna, D. Kodamala, S.A. Basha and S. Cole, *Next Mater.*, **8**, 100819 (2025); https://doi.org/10.1016/j.nxmate.2025.100819
17. S. Cole, S.A. Basha, B.V.N. Kumar, K. Srinivasarao, K. Daniel and S.V. Balasubramanyam, *Phys. Chem. Res.*, **14**, 173 (2026); https://doi.org/10.22036/pcr.2025.539879.2719
18. M. Karolewicz, H. Fuks and E. Tomaszewicz, *J. Therm. Anal. Calorim.*, **138**, 2219 (2019); https://doi.org/10.1007/s10973-019-08323-4
19. K. Souifi, O. Rejaiba, O. Amorri, B. Alzahrani, M.L. Bouazizi, M. Nasri, K. Khirouni and J. Khelifi, *J. Inorg. Organomet. Polym. Mater.*, **32**, 4515 (2022); https://doi.org/10.1007/s10904-022-02451-5
20. R.Y. Mudi, P.R.K. Pambi, V.L.K. Ganti and R. N.S.S.V.R, *Macromol. Symp.*, **393**, 1900214 (2020); https://doi.org/10.1002/masy.201900214
21. R.L. Frost, R. Scholz, A. López and Y. Xi, *Spectrochim. Acta A Mol. Biomol. Spectrosc.*, **124**, 243 (2014); https://doi.org/10.1016/j.saa.2014.01.053
22. H. Lamsaf, R. Fausto, B.F.O. Costa, J. Toyir, E.H. Elghadraoui and M. Ijjali, *Mater. Chem. Phys.*, **216**, 22 (2018); https://doi.org/10.1016/j.matchemphys.2018.05.060
23. S.V. Balasubramanyam, K.S. Rao, K. Daniel, S.A. Basha and S. Cole, *J. Phys. Chem. Res.*, **13**, 463 (2025); https://doi.org/10.22036/pcr.2025.507953.2645
24. X. Min, Z. Huang, M. Fang, Y.G. Liu, C. Tang and X. Wu, *Inorg. Chem.*, **53**, 6060 (2014); https://doi.org/10.1021/ic500412r
25. I. Kumar and A.K. Gathania, *J. Mater. Sci. Mater. Electron.*, **33**, 328 (2022); https://doi.org/10.1007/s10854-021-07301-7
26. K. Satyavathi, M.S. Rao, Y. Nagabhaskararao and S. Cole, *J. Mater. Sci. Mater. Electron.*, **28**, 12226 (2017); https://doi.org/10.1007/s10854-017-7038-8
27. V. Singh, A. Yadav, C.B. Annapurna Devi, A.S. Rao and N. Singh, *Optik*, **242**, 167264 (2021); https://doi.org/10.1016/j.ijleo.2021.167264
28. Y.N. Rajeev, K. Venkatarao, B.V.N. Kumar, L.B. Kumar and S. Cole, *Mater. Today Proc.*, **49**, A1 (2022); https://doi.org/10.1016/j.matpr.2021.12.554
29. Y. Wei, Z. Gao, S. Liu, S. Chen, G. Xing, W. Wang, P. Dang, A.A. Al Kheraif, G. Li and J. Lin, *Adv. Opt. Mater.*, **8**, 1901859 (2020); https://doi.org/10.1002/adom.201901859
30. N. Tejas, A. Princy, S.M.M. Kennedy, V. Mishra, M.I. Sayyed, T.A. Hanafy and S.D. Kamath, *Mater. Adv.*, **5**, 9756 (2024); https://doi.org/10.1039/D4MA00926F
31. M. Fhoula and M. Dammak, *J. Lumin.*, **210**, 1 (2019); https://doi.org/10.1016/j.jlumin.2019.01.058

32. B.V. Naveen Kumar, K. Venkata Rao, E. Basha Shaik, Y. Nirmal Rajeev, K. Ramachandra Rao and S. Cole, *Luminescence*, **37**, 1942 (2022); https://doi.org/10.1002/bio.4378
33. M. Khajuria, S.A. Bhat, R. Raina and P. Biswas, *J. Mater. Sci. Mater. Electron.*, **36**, 801 (2025); https://doi.org/10.1007/s10854-025-14860-6
34. A.M. Kelley and D.F. Kelley, *J. Phys. Chem. Lett.*, **13**, 11942 (2022); https://doi.org/10.1021/acs.jpclett.2c02677
35. P. Singh, H. Mishra and S.B. Rai, *Sci. Rep.*, **13**, 21221 (2023); https://doi.org/10.1038/s41598-023-46065-4
36. S.N. Ogugua, S.K.K. Shaat, H.C. Swart, R.E. Kroon and O.M. Ntwaeaborwa, *J. Alloys Compd.*, **775**, 950 (2019); https://doi.org/10.1016/j.jallcom.2018.10.090
37. B.V.N. Kumar, H.C. Swart and R.E. Kroon, *Opt. Mater. X*, **24**, 100355 (2024); https://doi.org/10.1016/j.omx.2024.100355
38. A.R. Beck, S. Das and J. Manam, *J. Mater. Sci. Mater. Electron.*, **28**, 17168 (2017); https://doi.org/10.1007/s10854-017-7645-4
39. T.C. Mohan, P.S. Dinesh, B.S.N. Devara, T.R. Raman and Y.C. Ratnakaram, *Luminescence*, **40**, e70288 (2025); https://doi.org/10.1002/bio.70288
40. S.A. Basha, K. Srinivasarao, K. Daniel, B.V. Naveen Kumar, Y.N. Rajeev and S. Cole, *Chem. Pap.*, (2026); https://doi.org/10.1007/s11696-026-05178-6
41. L. Han, Q. Zhang, J. Song, Z. Xiao, Y. Qiang, X. Ye, W. You and A. Lu, *J. Lumin.*, **221**, 117041 (2020); https://doi.org/10.1016/j.jlumin.2020.117041
42. A.K. Narasimhan, S.L. Balasubramanian and G. Krishnamurthi, *Mater. Lett.*, **300**, 130214 (2021); https://doi.org/10.1016/j.matlet.2021.130214